X-Ray Magnetic Circular Dichroism Measurements in Ni up to 200 GPa: Resistant Ferromagnetism

R. Torchio,[1,2] Y. O. Kvashnin,[1] S. Pascarelli,[1] O. Mathon,[1] C. Marini,[1] L. Genovese,[1,3] P. Bruno,[1] G. Garbarino,[1] A. Dewaele,[4] F. Occelli,[4] and P. Loubeyre[4]

[1]*European Synchrotron Radiation Facility, 6 Rue Jules Horowitz, BP220, 38043 Grenoble Cedex, France*
[2]*Dipartimento di Fisica "E. Amaldi," Universitá di Roma Tre, Via della Vasca Navale 84, I-00146 Roma, Italy*
[3]*Laboratoire de Simulation Atomistique, SP2M, UMR-E CEA/UJF-Grenoble 1, INAC, Grenoble, F-38054, France*
[4]*CEA, Bruyres le- Chtel, 91297 Arpajon Cedex, France*

(Received 4 May 2011; published 30 November 2011)

The structural stability of fcc Ni over a very large pressure range offers a unique opportunity to experimentally investigate how magnetism is modified by simple compression. *K*-edge x-ray magnetic circular dichroism (XMCD) shows that fcc Ni is ferromagnetic up to 200 GPa, contradicting recent predictions of an abrupt transition to a paramagnetic state at 160 GPa. Density functional theory calculations point out that the pressure evolution of the *K*-edge XMCD closely follows that of the *p* projected orbital moment rather than that of the total spin moment. The disappearance of magnetism in Ni is predicted to occur above 400 GPa.

DOI: 10.1103/PhysRevLett.107.237202 PACS numbers: 75.50.Cc, 62.50.−p, 78.20.Ls, 81.40.Vw

The appearance of ferromagnetism in Fe (bcc), Co (hcp), and Ni (fcc) metals is one of the most fundamental questions in solid-state physics. A qualitative understanding of the magnetic structure of metals relies on the Stoner theory, which points out the density of states at the Fermi level DOS(E_f) and the exchange interactions as the crucial factors at zero temperature. In the transition metals, the magnetic properties mainly arise from the partially filled spin-polarized 3*d* band which in turn is strongly related to the crystal structure and external factors such as temperature, magnetic field, and pressure. Therefore, exploring the stability limits of ferromagnetism as a function of these thermodynamical variables is fundamental to getting a deeper insight on its appearance. In particular, application of pressure is an effective way to study the complex interplay between magnetic, structural, and electronic degrees of freedom. The compression of interatomic distances leads to the broadening of the electronic bands (diminishing the importance of Coulomb correlations) and a decreased DOS(E_f). In the framework of the Stoner model, this means that, at sufficiently high compression, the condition for ferromagnetism stability is no longer satisfied and ferromagnetism is lost.

In iron, the collapse of ferromagnetism under pressure has been experimentally observed (see, for example, [1]) in correspondence to the bcc-hcp structural phase transition. In cobalt, the suppression of ferromagnetism occurs at the hcp-fcc transition in the 100–150 GPa range [2–6]. The pressure limit of ferromagnetism in Ni is still not established. No structural transitions have been reported in fcc Ni up to 150 GPa [7], and first-principles calculations predict fcc Ni to be stable up to 34 TPa [8]; being structurally stable over such a large pressure range, the case of Ni offers a unique opportunity to investigate how the simple compression of interatomic distance influences the magnetic properties.

Previous works [2,9] indicate a weak decrease of the *K*-edge x-ray magnetic circular dichroism (XMCD) signal under compression reaching 80% of the initial value at 70 GPa. Based on these measurements, nonmagnetic Ni was predicted above 250 GPa. All the available calculations agree in predicting a stable ferromagnetic fcc phase in nickel up to the Mbar range [10–12], with the spin magnetic moment slowly decreasing from the ambient value 0.6 μ_B/atom to 0.48 μ_B/atom around 300 GPa [11]. The Curie temperature (T_c) of Ni is 631 K at ambient pressure. A very recent work based on first-principles calculations and the partition function approach [13] predicts T_c to start decreasing sharply around 120 GPa and reaching ambient temperature around 160 GPa, when a paramagnetic state is thus expected. Two questions have motivated the present study: is the disappearance of magnetism in Ni within experimental reach and in the stability domain of the fcc structure? Are density functional theory (DFT) calculations reliable enough to predict the change of magnetization under pressure? We have tried to answer these questions by extending as much as possible the pressure range probed by magnetic measurements on Ni: up to 200 GPa, corresponding to a volume compression of 0.66. We have thus combined XMCD, x-ray absorption near edge structure (XANES), and x-ray diffraction measurements. Also, *ab initio* calculations have been performed to compare the pressure evolution of XMCD experimental output to that of the Ni *p* projected orbital and spin magnetic moments. Our results indicate that the pressure-induced decay of the *K*-edge XMCD signal is closely related to that of the *p*-state orbital moments rather than to that of the total magnetization as previously assumed in the literature [2,9].

High-purity polycrystalline Ni powder was charged in an amagnetic diamond anvil cell (DAC) equipped with beveled 75×300 culets diamonds [14]. No pressure-transmitting medium was used. For each pressure, the volume compression was measured on beam line ID27 at the European Synchrotron Radiation Facility (ESRF) [15]. As shown in the lower panel of Fig. 1, the x-ray diffraction measurements revealed a stable fcc structure in the whole pressure range of study. The pressure value was then calculated using the compression curve found in Dewaele *et al.* [7]. XANES and XMCD signals were recorded at the energy dispersive x-ray absorption spectroscopy beam line ID24 (ESRF) [16,17] at the Ni K edge ($E_0 = 8323$ eV). The highly focused beam (5 μm full width at half maximum) allowed to reach a pressure range so-far unexplored by x-ray absorption spectroscopy. Such a high pressure actually represents a record for magnetic measurements comparable to Mössbauer techniques [18] whose application is anyway limited to few elements (mainly Fe compounds). Figure 1 reports the normalized XANES (left) and XMCD (right) signals between ambient pressure and 200 GPa. The XMCD signal is obtained by taking the difference between x-ray absorption spectra measured using parallel (μ^+) and antiparallel (μ^-) orientations of the sample magnetization relative to the incident photon helicity.

The investigation of magnetism in the $3d$ metals using XMCD is generally carried out at the L edges, which directly probe d-symmetry final states. However, these edges are not accessible at high pressure in a DAC due to the opacity of the diamond anvil at such low energies. It is necessary instead to probe the K edges, making the experiment complex both from an experimental and interpretational point of view. K-edge XMCD measures the imbalance in the density of empty p valence states with quantum numbers $+m_l$ and $-m_l$. In the $3d$ metals, the K-XMCD signal is generally small ($\sim 10^{-3}$ or weaker). In addition, in a DAC, the x-ray beam is strongly attenuated by the anvils and the sample size must be of the order of a few microns so as to exceed 100 GPa pressure.

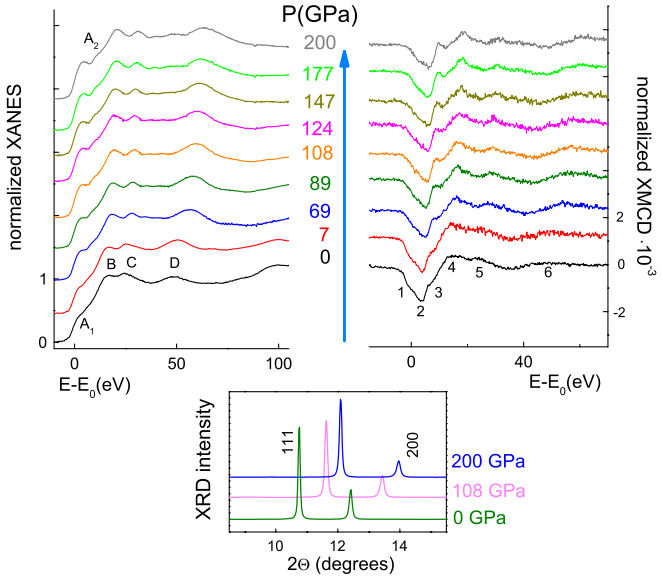

FIG. 1 (color online). Upper panel: Combined XANES (left) and XMCD (right) spectra in pure Ni up to 200 GPa ($E_0 = 8323$ eV). Lower panel: selected angle-dispersive XRD patterns up to 200 GPa.

As seen in Fig. 1, compression modifies both the XANES and XMCD features. For the XANES spectra (upper-left panel), the main changes are (i) an increase of the prepeak feature A_1, (ii) the appearance of a shoulder in the preedge region (A_2), and (iii) an inversion of the relative height of peaks B and C. The intensity enhancement of the A_1 feature, which originates from the quadrupolar $1s \rightarrow 3d$ transitions [19], has already been observed under pressure [2,9,20] in all the $3d$ metals and interpreted as an increase of $3d - 4p$ band overlap under compression. Features B, C, and D shift towards higher energies due to compression of the local structure [20]. For the XMCD spectra (upper-right panel), the main valley (2) gradually looses intensity ($-$ 34%) and the post edge peaks (3, 4, 5, and 6) become sharper. No sharp signal decay is observed between 120 and 160 GPa. Our results are thus in disagreement with the prediction of an abrupt pressure-induced paramagnetism at these pressures [13]. Finally, it is interesting to note that, whereas the energy position of features 1 and 2 does not evolve significantly with pressure, features 3–6 shift towards higher energies following the evolution of the XANES features, i.e., stemming from the compression of the local structure. This distinct pressure behavior allows us to roughly identify two energy regions in the XMCD spectra: the first region corresponds to a few eV around the absorption onset, mainly sensitive to the electronic density of empty states close to the Fermi level; the second energy region corresponds to beyond a few eV and is more directly linked to the local structure through single and multiple scattering of the photoelectron.

The XMCD signal at the K edge of $3d$ metals mainly arises from the spin-orbit coupling of the photoelectron in the final state. Theoretical approaches for the interpretation of K-edge XMCD signals based on multiple scattering [21–23] and band structure calculations using a tight-binding approximation [24] claim that the main contribution to the signal comes from the spin polarization of the d states and arises from the scattering of the photoelectron from the spin-orbit (SO) potential of the neighbors and of the absorber [25]. Such a view has led to the conclusion that the K-edge XMCD signal should be somehow proportional to the $3d$ magnetic moment, and its pressure evolution has been often compared to that of the total spin magnetization [2,9]. The orbital sum rule [24,26,27] directly relates the integrated K-edge XMCD to the expectation value of the p projected orbital moment. Based on an atomic approach and the dipolar approximation, its

application to the K edge of the $3d$ metals is limited by the assumption of energy-independent radial matrix elements $R = \langle 1s|r|4p\rangle$, which does not apply to the broad and delocalized p final states [21,26]. Because of the abovementioned reasons, it is quite difficult to extract absolute quantitative information on the magnetic moment from K-edge XMCD spectra. Nevertheless, as the E dependence of the matrix elements is smooth, XMCD reflects the p orbital polarization in differential form $d\langle L_z\rangle_p/dE$ [28,29]. We have checked this for the Ni case by comparing the orbital magnetization density of p states $dm_l(E) \equiv \sum_{n\mathbf{k}} \langle \Psi_l^{n\mathbf{k}}|\hat{l}_z|\Psi_l^{n\mathbf{k}}\rangle \delta(E - E_{n\mathbf{k}})$ to the differential XMCD $d_{\mathrm{XMCD}}(E) \equiv \sum_{n\mathbf{k}} [|\langle \Psi_{n\mathbf{k}}|\Pi^+|\Psi_{1s}\rangle|^2 - |\langle \Psi_{n\mathbf{k}}|\Pi^-|\Psi_{1s}\rangle|^2]\delta(E - E_{n\mathbf{k}})$, where $\Pi^{\pm}$ is the dipole interaction operator of an electron with a photon of right (left) helicity [29,30], using the PY-LMTO code [31,32] (see Fig. 2). Hence, the relative behavior of an integrated XMCD signal under pressure can be expected to be approximately proportional to that of the p orbital moment.

In order to shed light on the role of the different contributions and interpret the measured compression evolution of the K-edge XMCD signal, we performed a series of DFT + SO calculations over a wide range of compression (between $V_0^{\mathrm{exp}} = 10.95$ Å and 5.04 Å, corresponding to V/V_0 ranging from 1 to 0.46), using WIEN2K [33] and PY-LMTO codes, assuming a stable fcc structure up to the TPa range, as suggested in [8]. Different treatments of correlation effects have been probed using local density approximation (LDA + PW92 [34,35]) and generalized gradient approximation (GGA + PBE [36]) for the exchange correlation functionals in WIEN2K. The Brillouin zone integration was performed on the 28^3 (22^3) k-point grid.

Our calculations confirm that the spin polarization of the p states mainly originates from the hybridization of p and d bands. On the other hand, unlike in Ref. [24], where it was found that the p orbital moment (and K-edge dichroism) is mostly due to the $3d$ SO coupling, we find that the

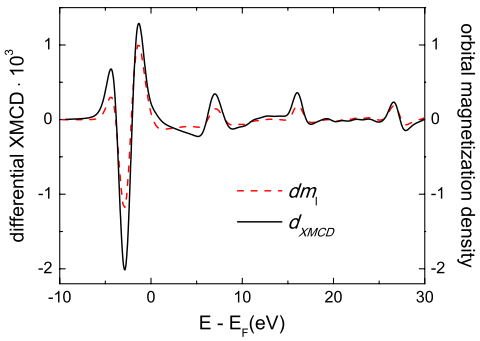

FIG. 2 (color online). Calculated orbital magnetization density of $4p$ states (right axis) and K-edge differential XMCD for bulk Ni (left axis). The calculations are performed for a zero-pressure unit cell using the PY-LMTO code. The curves are broadened with a Lorentzian function of 0.8 eV width.

$4p$ SO coupling contributes to 35% of the p orbital moment at ambient pressure and 50% at 0.66 relative compression [37]. In order to check the role of the quadrupolar contribution, Ni K-edge simulations were performed using the FDMNES code [38]. The results indicate that the inclusion of quadrupolar terms gives rise to a deviation of 3–5% in the whole pressure range of study; simulations using the tight-binding approach [24] had previously led to similar conclusions.

The ambient values obtained for the spin and orbital d moments and for the pressure evolution of the total spin moment are in good agreement with previous calculations and experiments [10–12,39]. The difference found in the ambient moments using different methods results to be quite small for the d spin and orbital moments (1–6%) but quite significant for the p spin and orbital moments ($\approx 20\%$). However, the slope of the linear compression-induced decay—the physical quantity we are interested in—is similar for each moment component using different methods. Interestingly, the p and d orbital moments behave very similarly with compression, whereas this is not the case for the p and d spin moments [40].

Our results indicate that orbital and spin magnetization terms keep decreasing continuously up to a compression of $V/V_0 \approx 0.6$, where a sharper decay leads to total and simultaneous extinction. The different methods applied are in qualitative good agreement but indicate different critical zero-moment volumes, ranging from $0.48V_0$ to $0.54V_0$. A similar variation in the calculated pressure of moment extinction is found in the case of cobalt [5]. In fact, the quantitative reliability of these methods at such high compression is limited, as the computed quantities are very small and vary very quickly; this fact underlines the importance of high-pressure experiments.

To compare the computed quantities to the experimental outputs, the XMCD signal has been integrated and normalized to the integral of the unpolarized absorption (XANES) $\mu_0 = (\mu^+ + \mu^-)/2$:

$$A_{\mathrm{XMCD}} \equiv \int_{E_1}^{E_2} dE(\mu^+ - \mu^-) / \int_{E_1}^{E_2} dE\mu^0.$$

The integral's interval has been chosen from the signal onset ($E_1 = -7$ eV) to four different upper limits E_2 between 4 and 15.5 eV, so as to take into account the broad character of the final p states (i.e., the absence of a white line). This energy range for the upper limit fully spans the transition zone between the energy region mainly sensitive to the electronic structure and the region mainly sensitive to the local structure. Then, the pressure evolutions of the A_{XMCD}, obtained in the 4 cases, were rescaled to their ambient values and compared. We found that the error due to the upper limit choice amounts to 4–12%, indicating that the pressure-induced decrease of A_{XMCD} does not change significantly with the energy interval. In Fig. 3(c), we plot the average between the pressure evolutions

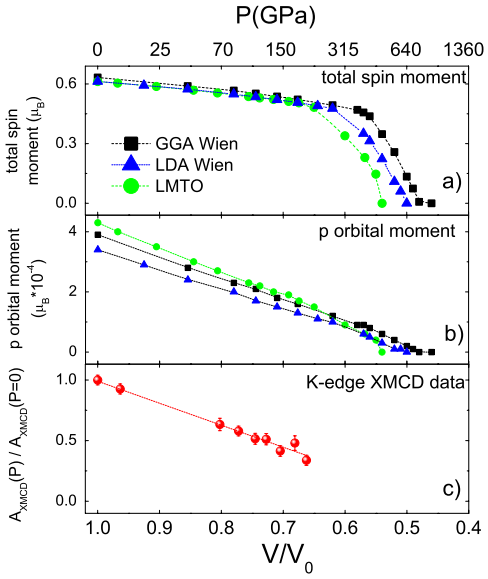

FIG. 3 (color online). Volume evolution of (a) the calculated total spin moment, (b) the p orbital moment, and (c) the normalized XMCD integral (A_{XMCD}). The nonlinear pressure scale in the top axis is calculated with the equation of state given in [7].

obtained using the four intervals; the error is chosen at each point as the maximum value between the error due to the integral upper limit choice and the error due to the signal noise ($\approx 5\%$).

Comparison with theoretical calculations for the total spin moment [Fig. 3(a)] and p orbital moment [Fig. 3(b)] reveals that the integral of the measured XMCD signal reduces by $\approx 60\%$ in the 0–200 GPa range, just like the p orbital moment, while the total spin moment shows a different behavior, decreasing by 20%.

In summary, we have extended up to 200 GPa the pressure range for combined magnetic and structural measurements, by measuring K-edge XMCD-XANES and x-ray diffraction (XRD) on pure Ni. The K-XMCD signal decreases continuously under compression and remains nonzero at 200 GPa, indicating the persistence of ferromagnetic order. This Letter demonstrates that today pressures of a few Mbar can be coupled to simultaneous magnetic and structural studies. DFT calculations were performed to compute spin and orbital moment components in compressed Ni, so far missing in the literature, allowing us to get a deep insight into their different behavior vs density. This study can lead to the following conclusions: (i) the pressure evolution of the nickel K-edge XMCD closely follows that of the p projected orbital moment and not that of the total spin magnetization; and (ii) the disappearance of magnetism in Ni is predicted to occur at pressures higher than 400 GPa. However, one cannot rule out a possible crystallographic phase transition or a transition to a paramagnetic state at ambient temperature and at lower pressure. Hence, further experimental investigations of the magnetic response of Ni under more extreme compressions appear necessary. The present approach is currently under upgrade, and the extension of magnetic measurements in the 300–400 GPa range and at low temperature—which would allow us to disentangle the moment suppression from T_c effects—looks promising.

We acknowledge Sebastian Pasternak for the technical support and Andrei Rogalev for fruitful discussions. The authors acknowledge the European Synchrotron Radiation Facility for provision of synchrotron radiation facilities (Proposal No. HS-3348).

[1] M. Nicol and G. Jura, Science **141**, 1035 (1963); O. Mathon *et al.*, Phys. Rev. Lett. **93**, 255503 (2004).
[2] V. Iota *et al.*, Appl. Phys. Lett. **90**, 042505 (2007).
[3] C. S. Yoo *et al.*, Phys. Rev. Lett. **84**, 4132 (2000).
[4] J. E. Saal *et al.*, J. Phys. Condens. Matter **22**, 096006 (2010).
[5] R. Torchio *et al.*, Phys. Rev. B **84**, 060403(R) (2011).
[6] N. Ishimatsu *et al.*, Phys. Rev. B **83**, 180409(R) (2011).
[7] A. Dewaele *et al.*, Phys. Rev. B **78**, 104102 (2008).
[8] A. K. McMahan and R. C. Albers, Phys. Rev. Lett. **49**, 1198 (1982).
[9] N. Ishimatsu *et al.*, J. Phys. Soc. Jpn. **76**, 064703 (2007).
[10] J. Xie *et al.*, J. Phys. Condens. Matter **12**, 8953 (2000).
[11] T. Jarlborg, Physica (Amsterdam) **385C**, 513 (2003).
[12] Y. S. Mohammed *et al.*, J. Magn. Magn. Mater. **322**, 653 (2010).
[13] Shun-Li Shang *et al.*, J. Appl. Phys. **108**, 123514 (2010).
[14] A. Dewaele *et al.*, Phys. Rev. Lett. **97**, 215504 (2006).
[15] M. Mezouar *et al.*, J. Synchrotron Radiat. **12**, 659 (2005).
[16] S. Pascarelli *et al.*, J. Synchrotron Radiat. **13**, 351 (2006).
[17] O. Mathon *et al.*, J. Synchrotron Radiat. **11**, 423 (2004).
[18] T. Mitsui *et al.*, J. Synchrotron Radiat. **16**, 723 (2009).
[19] J. E. Muller, O. Jepsen, and J. W. Wilkins, Solid State Commun. **42**, 365 (1982).
[20] C. R. Natoli, *EXAFS and Near Edge Structure III* (Springer, Berlin, 1984), p. 167.
[21] H. Ebert *et al.*, Z. Phys. B **73**, 77 (1988).
[22] A. Ankudinov and J. J. Rehr, Phys. Rev. B **52**, 10 214 (1995).
[23] C. Brouder, M. Alouani, and K. H. Bennemann, Phys. Rev. B **54**, 7334 (1996).
[24] J. Igarashi and K. Hirai, Phys. Rev. B **50**, 17 820 (1994).
[25] J. P. Rueff *et al.*, Phys. Rev. B **58**, 12 271 (1998).
[26] G. Y. Guo, J. Phys. Condens. Matter **8**, L747 (1996); Phys. Rev. B **55**, 11 619 (1997).
[27] B. T. Thole *et al.*, Phys. Rev. Lett. **68**, 1943 (1992).
[28] H. J. Gotsis and P. Strange, J. Phys. Condens. Matter **6**, 1409 (1994).
[29] V. N. Antonov, B. N. Harmon, and A. N. Yaresko, Phys. Rev. B **67**, 024417 (2003).

[30] L. Uba, S. Uba, V. N. Antonov, T. Ślezak, J. Korecki, and A. N. Yaresko, Phys. Rev. B **62**, 13 731 (2000).
[31] V. Antonov, B. Harmon, and A. Yaresko, *Electronic Structure and Magneto-Optical Properties of Solids* (Kluwer Academic, Dordrecht, 2004).
[32] A. Perlov, A. Yaresko, and V. Antonov, PY-LMTO (unpublished).
[33] P. Blaha *et al.*, WIEN2K, Vienna University of Technology, 2001.
[34] J. P. Perdew and Y. Wang, Phys. Rev. B **45**, 13 244 (1992).
[35] D. M. Ceperley and B. J. Alder, Phys. Rev. Lett. **45**, 566 (1980).
[36] J. P. Perdew, K. Burke, and M. Ernzerhof, Phys. Rev. Lett. **77**, 3865 (1996).
[37] This was checked with constrained calculations by fixing SO constants to zero on, alternatively, $4p$ and $3d$ states.
[38] Y. Joly, Phys. Rev. B **63**, 125120 (2001).
[39] O. Eriksson *et al.*, Phys. Rev. B **42**, 2707 (1990).
[40] See Supplemental Material at http://link.aps.org/supplemental/10.1103/PhysRevLett.107.237202 for the detailed calculations.